


Epidermal activation of Hedgehog signaling establishes an immunosuppressive microenvironment in basal cell carcinoma by modulating skin immunity

Sandra Grund-Gröschke¹, Daniela Ortner², Antal B. Szenes-Nagy¹, Nadja Zaborsky³, Richard Weiss¹, Daniel Neureiter⁴, Martin Wipplinger¹, Angela Risch¹, Peter Hammerl¹, Richard Greil³, Maria Sibilia⁵, Iris K. Gratz¹, Patrizia Stoitzner² and Fritz Aberger¹ 

¹ Department of Biosciences, Cancer Cluster Salzburg, Paris-Lodron University Salzburg, Austria

² Department of Dermatology, Venereology & Allergology, Medical University Innsbruck, Austria

³ IIIrd Medical Department, Salzburg Cancer Research Institute - Laboratory for Immunological and Molecular Cancer Research (SCRI-LIMCR), Paracelsus Medical University Salzburg, Cancer Cluster Salzburg, Austria

⁴ Institute of Pathology, Paracelsus Medical University Salzburg, Cancer Cluster Salzburg, Austria

⁵ Institute of Cancer Research, Comprehensive Cancer Center, Medical University of Vienna, Austria

Keywords

basal cell carcinoma; cancer immunotherapy; hedgehog/gli signaling; immune checkpoint molecules; neutrophils; regulatory T cells

Correspondence

F. Aberger, Department of Biosciences, Cancer Cluster Salzburg, University of Salzburg, Hellbrunner Strasse 34, 5020 Salzburg, Austria
Fax: +43 662 8044 - 183
Tel: +43 662 8044 5792
E-mail: fritz.aberger@sbg.ac.at

(Received 22 January 2020, revised 27 May 2020, accepted 26 June 2020, available online 21 July 2020)

doi:10.1002/1878-0261.12758

Genetic activation of hedgehog/glioma-associated oncogene homolog (HH/GLI) signaling causes basal cell carcinoma (BCC), a very frequent non-melanoma skin cancer. Small molecule targeting of the essential HH effector Smoothened (SMO) has proven an effective therapy of BCC, though the frequent development of drug resistance poses major challenges to anti-HH treatments. In light of recent breakthroughs in cancer immunotherapy, we analyzed the possible immunosuppressive mechanisms in HH/GLI-induced BCC in detail. Using a genetic mouse model of BCC, we identified profound differences in the infiltration of BCC lesions with cells of the adaptive and innate immune system. Epidermal activation of Hh/Gli signaling led to an accumulation of immunosuppressive regulatory T cells, and to an increased expression of immune checkpoint molecules including programmed death (PD)-1/PD-ligand 1. Anti-PD-1 monotherapy, however, did not reduce tumor growth, presumably due to the lack of immunogenic mutations in common BCC mouse models, as shown by whole-exome sequencing. BCC lesions also displayed a marked infiltration with neutrophils, the depletion of which unexpectedly promoted BCC growth. The study provides a comprehensive survey of and novel insights into the immune status of murine BCC and serves as a basis for the design of efficacious rational combination treatments. This study also underlines the need for predictive immunogenic mouse models of BCC to evaluate the efficacy of immunotherapeutic strategies *in vivo*.

1. Introduction

Basal cell carcinoma (BCC) of the skin represents a very common human cancer entity with around 3–4 million new cases diagnosed per year in the United States alone

[1]. The etiology of BCC is based on the persistent ligand-independent activation of hedgehog/glioma-associated oncogene homolog (HH/GLI) signaling, caused in the vast majority of cases by inactivating mutations in the HH receptor and pathway repressor

Abbreviations

BCC, basal cell carcinoma; DETC, dendritic epidermal T cell; GLI, glioma-associated oncogene homolog; HH, hedgehog; MDSC, myeloid-derived suppressor cell; NK, natural killer; PD, programmed death; PD-L, programmed death ligand; PTCH1, Patched-1; SMO, Smoothened; TAM, tamoxifen; TGF, transforming growth factor; Treg, regulatory T cells.

Patched-1 (PTCH1) or in fewer cases by activating mutations in the essential HH effector Smoothened (SMO). Under normal physiological conditions, HH/GLI signaling is actively repressed by PTCH1 in the absence of HH ligand. Pathway activation occurs upon binding of secreted HH protein to its receptor PTCH1, a twelve-transmembrane domain protein. Ligand binding results in the endocytic uptake of the PTCH1-HH complex, thereby allowing SMO—a G protein-coupled receptor-like transmembrane protein—to enter the primary cilium. Activation of SMO within the primary cilium triggers the formation of activator forms of GLI zinc-finger transcription factors. In response to their activation, GLI proteins translocate to the nucleus to induce HH target gene expression. In BCC, irreversible activation of HH signaling culminates in high levels of oncogenic GLI transcription factors, which initiate and promote tumor growth by continuous hyperactivation of HH target genes involved in proliferation, survival, angiogenesis, stemness and (de-) differentiation [2–12]. Although most BCC lesions are routinely removed by surgical excision, unresectable locally advanced and metastatic BCC require drug therapy. Small molecule inhibitors targeting SMO such as vismodegib and sonidegib have shown therapeutic efficacy in locally advanced and metastatic BCC, with overall response rates of 40–60 percent and complete responses in about 20 percent of patients [13–17]. However, despite the striking therapeutic efficacy of SMO inhibitors, their successful clinical use is limited and challenged by frequent *a priori* and acquired drug resistance, lack of durable responses, severe adverse effects and relapse of patients upon drug withdrawal. These limitations call for novel therapeutic regimens improving the response rates and durability of the therapeutic effect of HH inhibitors [1,18–22].

The recent breakthroughs in cancer immunotherapy that are based on our present understanding of how cancer cells evade the surveillance machinery of the adaptive and innate immune system have guided and paved the way to more efficacious, durable and even curative cancer therapies [23]. For instance, therapeutic antibodies targeting immune checkpoints such as programmed death-1/programmed death-ligand 1 (PD-1/PD-L1) signaling have been shown to re-instate the antitumoral immune response resulting in yet unprecedented therapeutic efficacy even in metastatic diseases [24–26]. Intriguingly, two reports have already demonstrated a therapeutic benefit of anti-PD-1 treatment for BCC patients and a combination of vismodegib and pembrolizumab is currently evaluated in a clinical trial (trial ID: NCT02690948) [27,28]. Together, these data raise the hope that rational combination

treatments targeting oncogenic HH/GLI and immunosuppressive mechanisms will synergistically improve the efficacy and durability of the therapeutic response of BCC patients with advanced or metastatic disease. A detailed understanding of the immune microenvironment of BCC as well as of the molecular players involved in establishing immune evasion is, therefore, of critical importance for the advancement of combination immunotherapy for unresectable BCC.

In this study, we strived to systematically investigate the molecular and cellular status of the immune microenvironment of HH/GLI-induced BCC, using a mouse model mimicking the genetic etiology of human BCC. We demonstrate that epidermal activation of HH/GLI signaling entails a variety of immunomodulatory mechanisms known to suppress immune recognition and subsequent eradication of neoplastic cells, thereby providing a basis for future combination treatments including immunotherapeutic drugs. In addition, we performed genomic sequencing of murine BCC-like lesions, which unlike in human BCC revealed no significant mutational burden, underlining the high need for predictive immunogenic murine BCC models to evaluate *in vivo* the efficacy of novel combinatorial immunotherapeutic treatments.

2. Material and methods

2.1. Mice

K14CreER^T (#005107) and *Ptch^{fl/fl}* (#012457) mice were obtained from the Jackson Laboratory (Bar Harbor, ME, USA) and genotyped according to the supplier's instructions. For tumor induction, 8-week-old mice and Cre negative *Ptch^{fl/fl}* animals were orally administered three times with 1 mg tamoxifen (TAM; Sigma, St Louis, MO, USA) dissolved in 10% ethanol/corn oil. Mice were analyzed 6 weeks after treatment, when they showed prominent pigmented lesions on the ears (also see Fig. 1A,B). All studies were performed on mice of both genders.

R26SmoM2:YFP [29] and *K5creER^T* mice [30] were bred to obtain *K5creER^T;R26SmoM2:YFP* (*SmoM2*) mice. Activation of *SmoM2* expression was accomplished by i.p. injection of 0.5 mg TAM citrate per day starting at postnatal day 14 for five consecutive days; Cre negative littermates received the same treatment. Mice started to develop macroscopically visible tumors 5 weeks after TAM administration.

For PD-1 blocking, TAM-treated *K14CreER^T;Ptch^{fl/fl}* mice were intraperitoneally injected every third day for 5 weeks with 250 µg of anti-PD-1 blocking antibodies

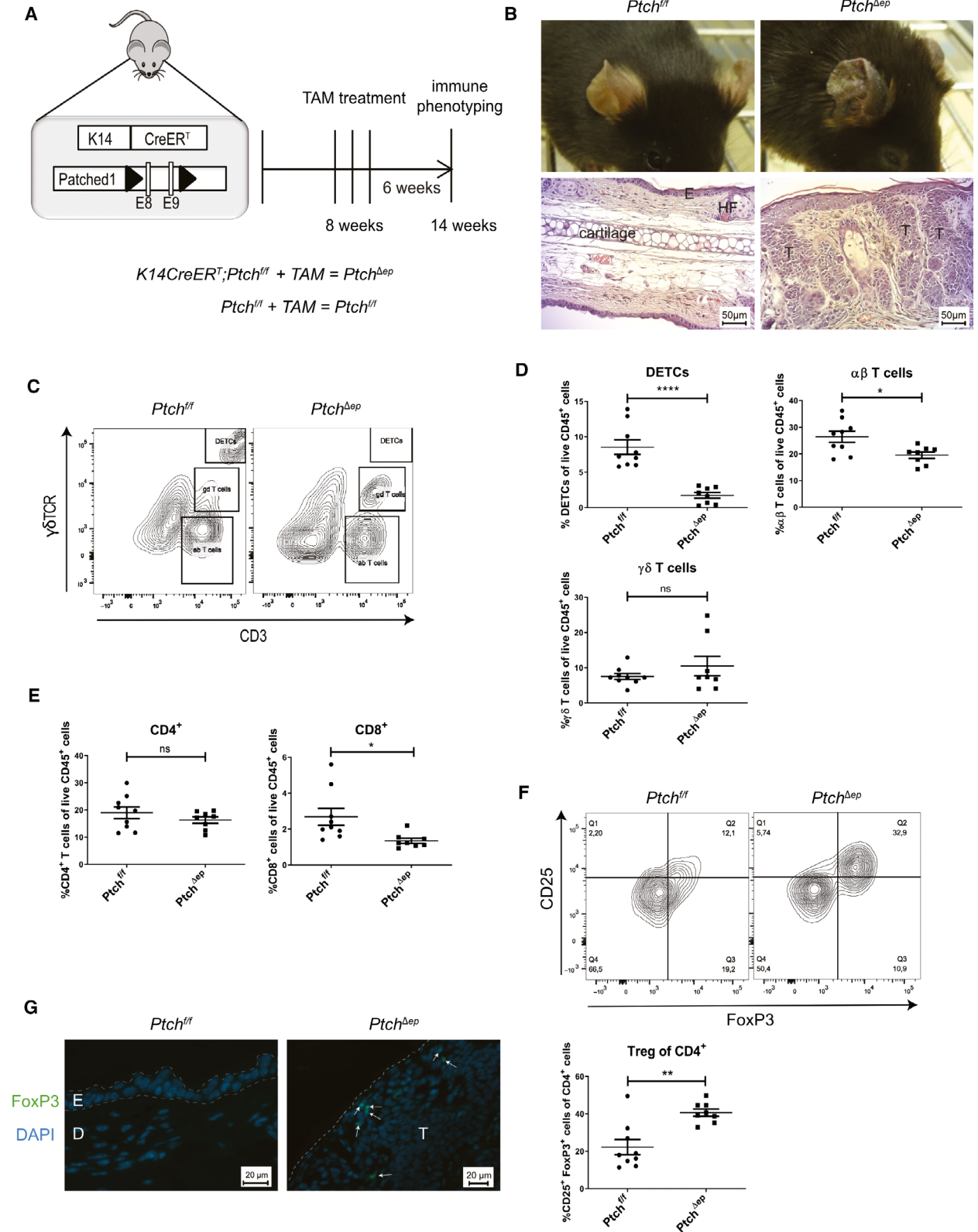


Fig. 1. Oncogenic HH signaling leads to altered T cell populations in BCC-like skin. (A) Schematic illustration of the *K14CreER^T;Ptch^{fl/fl}* (*Ptch^{Aep}*) mouse model and TAM treatment schedule. (B) Representative figures of the phenotype (upper panel) and H&E stainings (lower panel) of *Ptch^{fl/fl}* and *Ptch^{Aep}* mouse ears (scale bar 50 μ m). (C) Representative flow cytometry plots for T cell separation in mouse skin, using antibodies against $\gamma\delta$ TCR and CD3. (D–F) Flow cytometry analysis of (D) T cell populations, (E) CD4⁺ and CD8⁺ T cells and (F) CD25⁺ FoxP3⁺ Treg cells in *Ptch^{Aep}* ($n = 8$) and *Ptch^{fl/fl}* ($n = 9$) mouse skin. (F) Representative flow cytometry plot of CD25⁺ FoxP3⁺ Treg of CD4⁺ T cells in mouse skin (upper panel) and quantitative result of the flow cytometry analysis (lower panel). Cells were pre-gated for CD4. (G) Immunofluorescence analysis of mouse ear ($n = 3$) for FoxP3 (green) and DAPI (blue; scale bar 20 μ m). The arrows indicate the FoxP3⁺ cells. D, dermis; E, epidermis, HF, hair follicle; T, tumor mass. Statistical analysis for all experiments was performed with Student's *t* test. * $P < 0.05$, ** $P < 0.01$ and **** $P < 0.0001$.

(clone RMP1-14, BioXCell, West Lebanon, NH, USA), according to previously published papers [31–34]. A schematic overview is provided in Fig. 3A.

Neutrophils were depleted by intraperitoneal injection of anti-Ly6G antibodies (clone 1A8; BioXCell). After TAM treatment, *K14CreER^T;Ptch^{fl/fl}* mice received an initial dose of 400 μ g anti-Ly6G followed by thrice weekly injections of 100 μ g for 4 weeks, according to Coffelt *et al.* [35]. Successful depletion was verified weekly *via* flow cytometry staining of mouse blood. All studies were performed on mice of both genders.

Animal studies were performed in accordance with the institutional authorities and with the Federal Ministry of Science, Research and Economy (BMFWF-66.012/0016-WF/V/3b/2015 and BMFWF-66.011/0030-II/3b/2014).

2.2. Flow cytometry

For flow cytometry analysis of *K14CreER^T;Ptch^{fl/fl}* and control mice, the skin was digested for 45 min at 37 °C with 2 mg·mL⁻¹ collagenase XI, 0.5 mg·mL⁻¹ hyaluronidase and 0.1 mg·mL⁻¹ DNase in Dulbecco's Modified Eagle Medium (all from Sigma). Skin cell suspensions were filtered through 70- μ m cell strainer (Corning, Corning, NY, USA). Cells were stained with directly conjugated antibodies for 30 min at 4 °C in the dark. Separation of dead cells was accomplished with fixable viability dye eFluor 780, eFluor 520 or eFluor 506 (dilution 1 : 1000; Thermo Fisher Scientific, Waltham, MA, USA). To separate immune cells from other skin cells, CD45 as pan-leukocyte marker was included in all skin panels. Cells were fixed by using the Foxp3/transcription factor staining buffer set (Thermo Fisher Scientific) followed by intracellular staining. All experiments were performed on the BD FACS Canto II (BD Biosciences, Franklin Lakes, NJ, USA). For data analysis, the BD FACSDiva™ and the FLOWJO® software (BD Biosciences) were used.

For flow cytometry analysis of *SmoM2* mice, the ear skin was cut into small pieces and digested with 0.15 mg·mL⁻¹ Liberase™ and 0.12 mg·mL⁻¹ DNase I

(both Roche Diagnostics, Indianapolis, IN, USA) for 45 min at 37 °C and pressed through 100- μ m cell strainers (BD Biosciences). Nonspecific FcR-mediated antibody staining was blocked with anti-CD16/32 (2.4G2, in-house from hybridoma supernatant or from BD Biosciences) for 15 min at 4 °C. Cells were stained with directly conjugated antibodies for 15 min at 4 °C in the dark. Dead cells were excluded with 7-AAD (BD Biosciences) or fixable viability dye eFluor® 780 (Thermo Fisher Scientific). To separate immune cells from other skin cells, CD45 as pan-leukocyte marker was included in all skin panels. Cells were fixed by using the Foxp3/transcription factor staining buffer set (Thermo Fisher Scientific) or the Cytofix/Cytoperm™ kit (BD Biosciences) followed by intracellular staining. All experiments were performed on the BD FACS Canto II (BD Biosciences). For data analysis, the FLOWJO® software (BD Biosciences) was used.

Antibodies used for flow cytometry are listed in Table S1.

2.3. Quantitative PCR

Total RNA isolation and qPCR analysis of mRNA expression was carried out as describes previously [36]. The quantity and quality of isolated RNAs were assessed by Agilent Bioanalyzer 2200 system (Agilent Technologies, Santa Clara, CA, USA). qPCR was done on Rotor-Gene Q (Qiagen, Hilden, Germany) by using the GoTaq (Promega, Madison, WI, USA) or the Luna (NEB, Ipswich, MA, USA) qPCR master mix. Details about primers used in the study are listed in Table S2.

Total RNA from *SmoM2* mouse skin was isolated with TRIZOL (Thermo Fisher Scientific). Genomic DNA was removed using the RapidOut DNA removal kit (Thermo Fisher Scientific). Random primed cDNA was prepared with the Superscript II RNase H-reverse transcriptase (Thermo Fisher Scientific). mRNA expression was examined with quantitative PCR analysis by using the Brilliant III Ultra-fast qPCR Master Mix (Agilent Technologies). Information about the primers used is listed in Table S3.

2.4. Luminex cytokine profiling

Mouse dorsal skin was homogenized with the Ultra-Turrax® (IKA, Staufen, Germany) in PBS supplemented with protease inhibitor (Sigma) and filtered through Corning® Costar® Spin-X® Plastic Centrifuge Tubes (Sigma). For cytokine profiling, the ProcartaPlex™ multiplex system (Thermo Fisher Scientific) was used. The array analyses were carried out according to the supplier's instructions. Measurement was performed on the Magpix instrument (Luminex corp, Austin, TX, USA), and the analysis was done with the PROCARTAPLEX ANALYST 1.0 software (Thermo Fisher Scientific).

2.5. Histological analysis and immunofluorescence

Mouse ears were fixed overnight in 4% paraformaldehyde before paraffin embedding. 4- μ m sections from paraffin-embedded tissue were prepared for hematoxylin and eosin and immunofluorescence staining. Before staining, samples were deparaffinized and sections were blocked for 1 h in 1% BSA. For immunofluorescence staining, slides were incubated overnight with antibodies against CD8, FoxP3, PD-1 and Ly6G. For intracellular staining of FoxP3, Triton X-100 (Sigma) was added to a final concentration of 0.1%. Alexa 488- or Alexa 555-conjugated secondary antibodies were used for detection. Slides were mounted with Fluoroshield Mounting Medium with DAPI (Abcam, Cambridge, UK). Antibodies used for staining and detection are listed in Table S4. All pictures were taken on a Zeiss Axio Observer Z1 microscope (Carl Zeiss, Oberkochen, Deutschland) using ZEN 2.6 software (Carl Zeiss).

For quantification of the tumor area after neutrophil depletion, representative pictures from ears of three control and three tumor mice were quantified with the ImageJ software by three independent researchers in a blinded manner.

Immunohistochemistry of human BCC was done on FFPE tissue of eight different skin specimens with diagnosis of BCC [six female and two male patients, median age of 78.5 years and major localization of face ($n = 5$), trunk and extremities ($n = 3$)]. In brief, 4- μ m sections were mounted on glass slides, deparaffinized with graded alcohols, and stained using the primary antibodies listed in the Table S4, with pretreatment using pH 6.1 (FOXP3) or pH9 (all other antibodies) antigen retrieval buffer (Agilent Dako, Santa Clara, CA, USA). The immunohistochemical stainings were performed on a Benchmark Ultra

platform with the OptiView (PD-1 and PD-L1) or Ultraview (CD4, CD8, CD15 and FOXP3) DAB IHC detection kit (Ventana, Tucson, AZ, USA). For double IHC stainings, the first (PD-L1 or PD-1) and second (PD-L1: CD8 or PD-1: CD4, CD8 and FOXP3) antibodies were sequentially detected with the DAB (brown color) and Fast-Red (red) chromogen detection kit (Ventana).

2.6. Mouse whole-exome sequencing

Mouse genomic DNA was isolated from ear tissue using the DNeasy Blood and Tissue kit (Qiagen). Isolated genomic DNA was sheared with the Covaris M220 (Covaris, Woburn, MA, USA). DNA was subjected to whole-exome library generation [SureSelect^{XT} Mouse All Exon Kit; 49.6 megabases (Agilent)], which were sequenced 100 bp paired-end on the Illumina platform NextSeq 550 using the NextSeq 500/550 v2.5 kit (Illumina, San Diego, CA, USA). Sequencing reads were mapped to mouse reference genome (UCSC mm10) using Burrows-Wheeler Aligner with default settings (BWA-MEM v0.7.12-R1039) [37]. Duplicate removal was performed with default parameters using PicardTools (v2.10.3, <http://broadinstitute.github.io/picard/>). Alignments were preprocessed including local realignment around indels, and base quality recalibration was performed using Genome Analysis Tool Kit (GATKv3.7; all with default parameters) [38]. For somatic mutation calling (SNVs, Indels), each tumor sample (*K14CreER^T;Ptc1^{fl/fl}*) was compared with three *Ptc1^{fl/fl}* mice. Subsequently, all unique SNVs and indels were called. Mpileup file generation was done by SAMTOOLS (v1.5; parameter `-B -q 1`) [39], VARSCAN2 (v2.4.3) was used for somatic variant calling (`-min-coverage-normal 5 -min-coverage-tumor 5 -min-var-freq 0.05 -somatic-P-value 0.05 -strand-filter 1`), and filtering of high confidence calls was performed according to Basic Protocol 2 published by Koboldt *et al.* [40]. Variants were annotated using ANNOVAR (version 2017Jul16) [41]. All programs were executed following the authors' recommendations. Nonsynonymous exonic SNVs and Indels were considered. All remaining mutations were individually checked for accuracy using Integrative Genomics Viewer (IGV) version 2.4.2. [42,43]. For Copy Number Variations (CNVs) detection, depth of coverage was calculated for each exome target region using Varscan copynumber and Varscan copycaller. Coverage data were then analyzed using the R (version 3.6.1) package DNACOPY (version 1.58.0) using the circular binary segmentation algorithm (CBS) to segment DNA copy number data and identify genomic regions with abnormal copy number [44].

2.7. Alternative activation of mouse bone marrow-derived macrophages

Mouse bone marrow cells were isolated from the femoral bones and after red blood cell lysis grown in L929 fibroblast-conditioned medium (L929-sup, made in house) for 10 days at 7% CO₂. Afterward, bone marrow macrophages were alternatively activated with 50 ng·mL⁻¹ recombinant mouse IL4 (Immunotools, Friesoythe, Germany) for 24 h.

2.8. Statistical analysis

Significant differences between two groups were determined using an unpaired two-tailed Student's *t* test. Values are given as means (± SEM) and were analyzed by GRAPHPAD PRISM® 8 (GraphPad, San Diego, CA, USA). For human BCC stainings, the statistical analysis was performed with the IBM Corporations (Armonk, NY, USA) SSPS Statistics software. Here, the Levene test was used prior the *t* test. *P* values of < 0.05 were considered significant, and *P* values have been labeled and designated as follows: **P* < 0.05, ***P* < 0.01, ****P* < 0.001 and *****P* < 0.0001.

3. Results

3.1. Oncogenic HH/GLI signaling alters T cell populations in mouse BCC-like skin

The patients' response to cancer immunotherapy correlates with high mutational burden of the cancer tissue, presumably due to increased immunogenicity as a consequence of neoantigen expression [45,46]. Intriguingly, genomic sequencing of human BCC revealed that HH/GLI-driven skin cancers display an exceptionally high mutational burden with an average of 65 mutations per megabase [47], suggesting that BCC is likely to represent an immunogenic cancer entity. We, therefore, hypothesize that oncogenic HH/GLI signaling drives BCC growth by suppressing the antitumoral immune response and possibly, also by recruiting inflammatory cells with tumor-promoting function. Although single case and prove-of-concept studies have suggested that immunotherapeutic approaches can be successful in BCC [27,28], very little is known about how oncogenic HH/GLI signaling regulates tumor immunity in this cancer entity. To investigate the immunological modulation of BCC-like tumors in mouse skin in response to ligand-independent Hh/Gli activation, we treated 8-week-old *K14CreER^T;Ptch^{fl/fl}* (*Ptch^{Aep}*) mice with TAM to induce irreversible Hh/Gli activation and BCC-like

tumor formation, respectively. TAM-treated, Cre negative animals (*Ptch^{fl/fl}*, controls) were used as controls (Fig. 1A). In agreement with previous reports [48,49], mice with epidermal-specific deletion of *Ptch1* displayed a hyperproliferative BCC-like phenotype that was most prominently observable on the ears (Fig. 1B).

To analyze alterations of adaptive immune cells in tumor lesions of *Ptch^{Aep}* mice, we performed flow cytometry analysis of skin T cell populations. Viable CD45⁺ cells were gated for CD3 versus γδTCR, resulting in three distinct T cell populations with CD3⁺ γδTCR⁻ cells representing αβ-T cells, CD3⁺ γδTCR⁺ cells representing γδ-T cells and cells that showed very high expression of both markers known as dendritic epidermal T cells (DETCs; Fig. 1C). Interestingly, αβ-T cells and DETCs were decreased in *Ptch^{Aep}* mice in comparison with TAM-treated control mice, whereas the γδ-T cells remained unchanged (Fig. 1D). We validated these results by analyzing *K5creER^T;SmoM2* (*SmoM2*) BCC mice [36] expressing constitutively active oncogenic SMO in the epidermis after TAM injection. As shown in Fig. S1A, CD3⁺ and CD3^{high} (DETC) T cells were also reduced in lesional skin of *SmoM2* mice compared to controls (Fig. S1A).

Having shown that αβ-T cells were decreased in skin tumors, we next addressed whether this applies to CD8⁺ or CD4⁺ T cell subsets. Gating for both markers revealed that cytotoxic CD8⁺ T cells were slightly lowered in the skin of tumor-bearing mice, whereas the CD4⁺ T cell population stayed unaffected (Fig. 1E). Of note, this CD8 decrease could be confirmed in *SmoM2* BCC mice. However, in contrast to *Ptch^{Aep}* mice CD4⁺ T cells were increased in *SmoM2* mice (Fig. S1B). Whether the differences between the two murine BCC models are a due to overexpression of the mutant *SmoM2* oncogene, which itself might be immunogenic or a result of SMO-independent roles of *Ptch1* as dependence receptor [50] and binding partner cell cycle regulators such as Cyclin B [51] remains to be addressed. However, since nine out of 10 patients present inactivating mutations in *PTCH1* [1], we focused on a detailed and comprehensive analysis of the Patched1-deletion model of BCC.

Regulatory T cells (Treg) cells play a pivotal role in cancer immune evasion by suppressing the antitumoral immune response through different mechanisms such as the production of immunosuppressive cytokines [52,53]. Although the percentages of CD4⁺ lymphocytes were not changed in *Ptch^{Aep}* mice, we asked whether CD4⁺ FoxP3⁺ CD25⁺ Treg cells were altered. Notably, and as shown in Fig. 1F, FoxP3⁺ Tregs were strongly increased in mouse skin tumors compared to

nonlesional control skin. We analyzed by qPCR *FoxP3* expression in *SmoM2* mice and found elevated *FoxP3* transcript levels compared to control mice, suggesting that BCC lesions from *SmoM2*-expressing mice comprise elevated Treg cell numbers similar to *Ptch1*-deficient tumors (Fig. S1C). To determine the localization of Treg cells, we performed immunofluorescence staining of *Ptch^{Aep}* mouse ears. We found Treg cells to be localized in intra- and peri-tumoral regions, suggesting a possible role of Tregs in immunosuppression of the BCC microenvironment (Fig. 1G). We confirm Treg infiltration in the stromal compartment of human BCC and show that *FoxP3*⁺ cells do only rarely if at all co-express with the immune checkpoint PD-1 (Fig. S2A).

3.2. Increased immune checkpoint expression in mouse BCC-like skin

Having shown increased levels of immunosuppressive Tregs in mouse BCC-like skin, we next addressed the question of whether additional immunoregulatory mechanisms may support tumor immune escape. To this end, we performed a systematic screen for known immune checkpoints [54] *via* quantitative PCR of mouse BCC-like and control skin. Interestingly, we found *Pd-1* and its ligands *Pd-11* and *Pd-12* as well as *Tigit*, *Tim3*, and *Cd226* to be significantly upregulated in skin tumors, whereas *Lag3* and *Cd96* were not significantly changed compared to control skin (Fig. 2A). In addition, we confirmed upregulation of *Pd-11* mRNA levels in tumor lesions of *SmoM2* mice (Fig. S1D).

Given the clinical relevance of the PD-1/PD-L1 axis in cancer immunotherapy [54–58], we analyzed PD-1 expression on skin T cells of *Ptch^{Aep}* and control mice. As shown in Fig. 2B, on average 20% of all T cells expressed PD-1 in tumor lesions of *Ptch^{Aep}* mice, whereas these cells were virtually absent in control skin

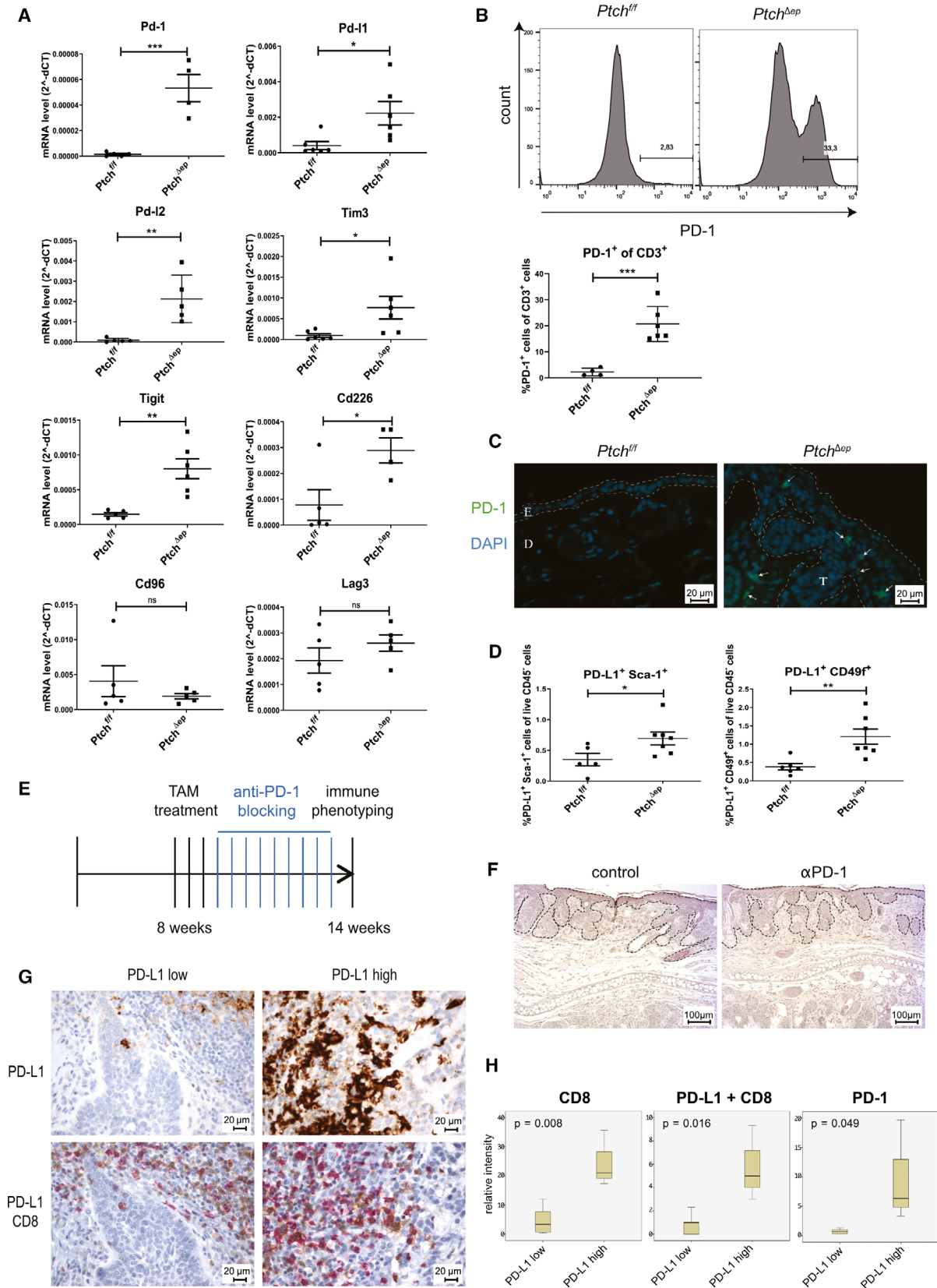
(Fig. 2B). Flow cytometry analysis revealed that both CD4⁺ and CD8⁺ T cells express PD-1, although the data did not reach statistical significance due to low mouse numbers in this analysis (Fig. S2B). To determine the *in situ* localization of PD-1-positive cells in the skin, we performed immunofluorescence staining of mouse ears. We found most PD-1⁺ cells to be located adjacent or within the epithelial tumor compartment (Fig. 2C).

We next performed double stainings of human BCC samples for PD-1 and either CD4 or CD8. We show that a fraction of both CD4⁺ and CD8⁺ T cells, which have infiltrated the tumor stroma, also express PD-1. Of note, we detected CD8⁺ PD-1⁺ cells in the stroma as well as in the actual tumor nodules, while CD4⁺ PD-1⁺ exclusively localized to the tumor microenvironment (Fig. S2C).

Intriguingly, expression of the PD-1 ligand PD-L1 in mouse tumors was mainly found in the Sca-1⁺ and/or CD49f⁺ epithelial compartment of BCC-like lesions, suggesting cell-autonomous induction of this immune inhibitory molecule in response to oncogenic Hh/Gli activation in epidermal cells (Fig. 2D), consistent with a recent study showing direct GLI-mediated PD-L1 activation in a murine organoid model of Gli2-driven gastric cancer [59].

Having shown that PD-1 is upregulated on skin T cells of *Ptch^{Aep}* mice, we set out to test whether re-activation of the antitumor immune response *via* anti-PD-1 immune checkpoint inhibition results in tumor regression. For this purpose, we injected TAM-treated *K14CreER^T;Ptch^{fl/fl}* with anti-PD-1 blocking antibodies (Fig. 2E). However, and unlike in human case studies, anti-PD-1 treatment was unable to reduce the tumor burden of *Ptch^{Aep}* mice (Fig. 2F and Fig. S3A). Analysis of the immune infiltrate of the skin *via* flow cytometry did not reveal significant alterations in the immune cells following PD-1 therapy (Fig. S3B). Since the response to immune checkpoint inhibition

Fig. 2. Increased immune checkpoint expression in BCC tumors. (A) qPCR analysis of mouse skin (*n* for *Pd-1* and *Cd226*: *Ptch^{fl/fl}* = 5 and *Ptch^{Aep}* = 4, for *Pd-11* and *Tim3*: *Ptch^{fl/fl}* = 6 and *Ptch^{Aep}* = 6, for *Pd-12* and *CD96*: *Ptch^{fl/fl}* = 5 and *Ptch^{Aep}* = 5, and for *Tigit*: *Ptch^{fl/fl}* = 5 and *Ptch^{Aep}* = 6). (B) Representative flow cytometry plot showing PD-1 expression on CD3⁺ T cells in mouse skin (upper panel) and flow cytometry analysis of PD-1 expression on CD3⁺ T cells (lower panel); *Ptch^{fl/fl}* *n* = 4 and *Ptch^{Aep}* *n* = 6). (C) Immunofluorescence analysis of murine ear skin stained for PD-1 (green) and DAPI (blue). The arrows highlight PD-1⁺ cells (scale bar 20 μm). (D) Flow cytometry analysis of PD-L1 expression on CD45⁻ Sca-1⁺ (*Ptch^{fl/fl}* *n* = 5 and *Ptch^{Aep}* *n* = 7) and CD49f⁺ (*Ptch^{fl/fl}* *n* = 6 and *Ptch^{Aep}* *n* = 7) keratinocytes in mouse skin. (E) Treatment schedule of PD-1 blocking in previously TAM-treated *K14CreER^T;Ptch^{fl/fl}* BCC mice. (F) Representative images of H&E staining of ear skin of *Ptch^{Aep}* mice treated with anti-PD-1 blocking antibody or untreated (*n* = 4 per group). The dashed lines mark the tumor area (scale bar 100 μm). (G) Representative immunohistochemical stainings of human BCC skin sections for PD-L1 (brown) alone and together with CD8 (red) nuclei are stained in blue. The samples were divided by PD-L1 low (*n* = 5) and high (*n* = 3) expression (scale bar 20 μm). (H) Quantification and statistical analysis of the CD8 and CD8 plus PD-L1 and PD-1 expression from PD-L1 low (*n* = 5) and high (*n* = 3) BCC. D, dermis; E, epidermis; T, tumor mass. Statistical analysis was performed with Student's *t* test except for (H), which was analyzed with the Levene test to prior *t* test. For (H), the whiskers show the minimum and maximum of data points. **P* < 0.05, ***P* < 0.01 and ****P* < 0.001.



correlates with mutational burden [45], we hypothesized that the lack of sufficient immunogenic mutations in our murine model of BCC may account for the failure of PD-1 therapy. Therefore, we performed whole-exome sequencing (complete mouse exome coverage 49.6 Mb) of mouse BCC-like lesions ($n = 3$) and control skin ($n = 3$) to survey the mutational landscape of *Ptch*^{Aep} tumor lesions. As shown in Table S5, we were unable to identify any mutations in two of three mice. One mouse tumor showed two mutations with unknown immunological consequence (Table S5). Furthermore, analysis of the copy number variations revealed minor negligible chromosomal alterations in all three mice analyzed (Fig. S4). Based on these data, we propose that *Ptch*^{Aep} tumors do not express neoantigens and, thus, are likely nonimmunogenic, although we cannot exclude the possibility of epigenetic re-activation of endogenous retroviral sequences [60]. In summary, the lack of additional mutations underlines the need for next-generation immunogenic mouse models of HH/GLI-driven skin cancer to evaluate immunotherapeutic strategies.

To show the relevance of these murine data to human pathophysiology, we performed immunohistochemical staining of human BCC specimen for CD8 and PD-L1. We subdivided the samples according to their PD-L1 expression in PD-L1 low and high (Fig. 2G). Thereby, we revealed that PD-L1 low samples showed a definable inflammation mostly in the peri-tumoral regions, while PD-L1 high samples showed marked immune infiltration of the tumor. Here, double staining of PD-L1 and CD8 showed a pronounced infiltration of PD-L1 high BCC tumors with CD8⁺ T cells together with focal PD-L1 expression on tumor cells in close proximity to CD8⁺ T lymphocytes, suggesting inhibition of cytotoxic T cells by PD-L1 expressing BCC cells *via* immune checkpoint signaling (Fig. 2G,H). In addition, human BCC expressing high levels of PD-L1 present a marked increase in infiltrating PD-1⁺ cells in the tumor microenvironment (Fig. 2H).

3.3. Mouse BCC-like skin displays an altered cytokine and chemokine expression profile

Having shown that largely unmutated *Ptch*^{Aep} lesions comprise altered T cell populations in comparison to *Ptch*^{fl/fl} skin, we hypothesized that also the cytokine and chemokine expression profiles differ between tumor lesions and control mice. We, therefore, performed by qPCR analysis and Luminex profiling a systematic mRNA and protein expression analysis of tumor and control skin for known immune-modulating

Table 1. Cytokine and chemokine expression profiles in murine BCC. nd, not determined.

Gene name	mRNA		Protein	
	Fold change	P-value	Fold change	P-value
Cytokines				
Il10	4.2	0.0523	nd	nd
Tgfβ	4.5	0.0039	nd	nd
Il1β	13.4	0.0024	3.4	0.1036
Ifnγ	7.8	0.0011	nd	nd
Il17	27.5	0.0098	nd	nd
Gmcsf	3.9	0.0104	1	0.9949
Inos	5.6	0.0425	nd	nd
Cox2	2.2	0.0747	nd	nd
Tslp	47.3	0.0710	2.6	0.0010
Tnf	2.2	0.0688	2.6	0.0083
Chemokines				
Mip-2	nd	nd	1.2	0.6193
Ena78	13.1	0.0003	1.4	0.4529
Gro-α	nd	nd	1.5	0.3141
Ccl2/Mcp-1	17	0.0418	4.6	0.0284
Ccl3/Mip-1α	3.8	0.0125	4.1	0.0161
Ccl7/Mcp-3	nd	nd	2.5	0.2955
Cxcl10/lp-10	nd	nd	1.1	0.9148

cytokines and chemokines (for summary, see Table 1). Of note, we found increased levels of several immunosuppressive cytokines such as *Tslp*, transforming growth factor β (*Tgfβ*), *Il10*, and *Inos* as well as of pro-inflammatory cytokines such as *Tnfα*, *Il1β*, *Ifnγ*, and *Il17* in tumor lesions compared to control skin. Furthermore, BCC-like lesions expressed elevated levels of immune cell attracting chemokines such as *Ccl2*, *Ccl3*, and *Ena78* [61,62]. We observed similar changes in cytokine/chemokine expression profiles in *SmoM2* BCC mice (Fig. S5). We conclude that persistent Hh/Gli signaling in epidermal cells induces pronounced changes in the expression of immune-modulatory and chemoattractant factors that contribute to the formation of an immunosuppressive tumor microenvironment, including shifts of T lymphocyte and possibly also myeloid cell populations.

3.4. Oncogenic HH signaling leads to altered innate immunity in mouse BCC-like skin

Having demonstrated that Hh/Gli signaling in mouse BCC-like tumors results in a significant increase in chemokine levels such as *Ccl2* and *Ccl3*—two well-known chemoattractants for innate immune cells [62,63]—we next analyzed quantitatively and qualitatively by flow cytometry analysis, whether epidermal Hh pathway activation results in changes of the innate immune cell population. To this end, we gated myeloid

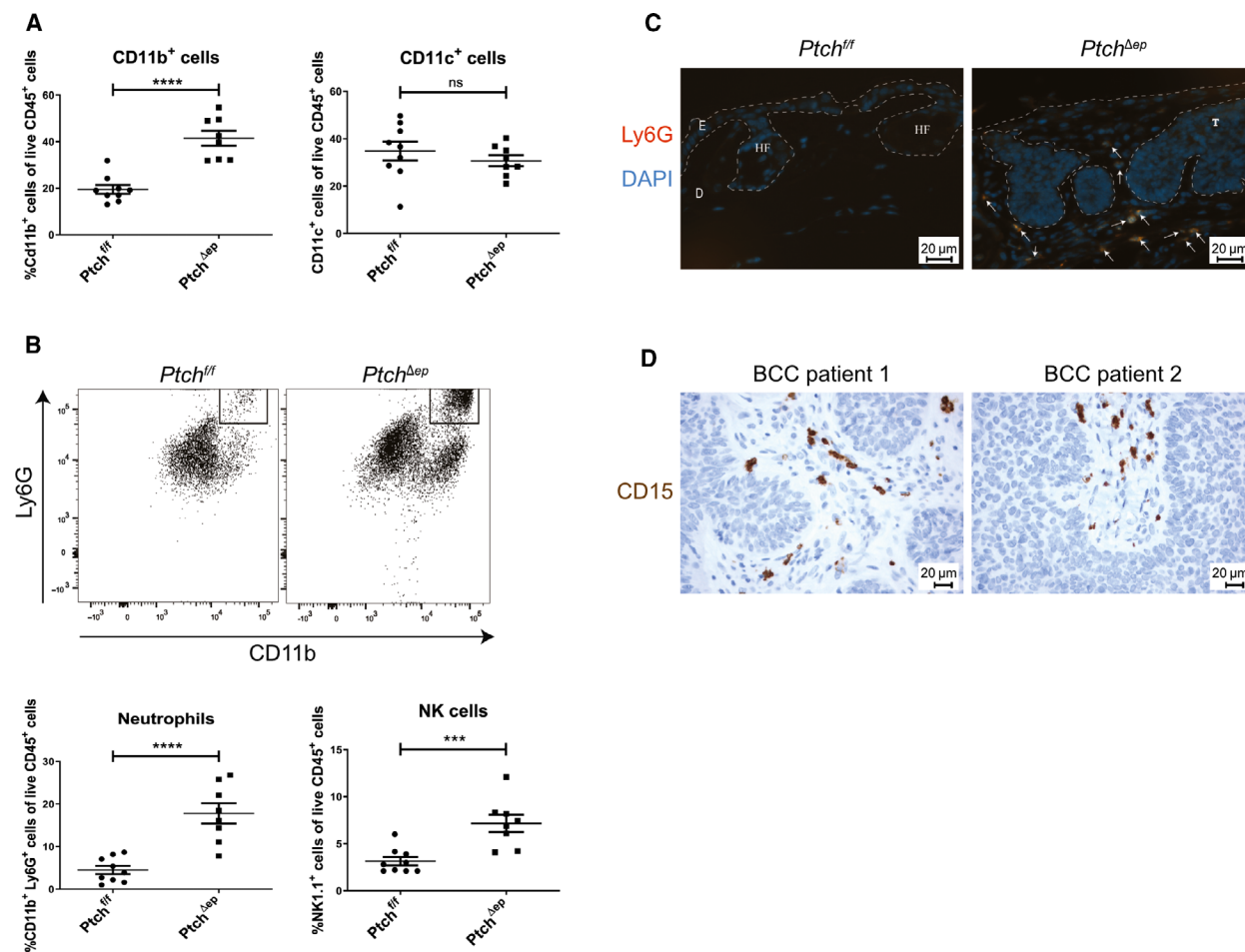


Fig. 3. Oncogenic HH signaling leads to altered innate immunity in BCC. (A) Flow cytometry analysis of murine skin for CD11b and CD11c expression in *Ptch^{Δep}* ($n = 8$) and *Ptch^{fl/fl}* control ($n = 9$) mice. (B) Representative flow cytometry plots for expression of Ly6G and CD11b (upper panel) and flow cytometry analysis for Ly6G and NK1.1 expression (*Ptch^{fl/fl}* $n = 9$ and *Ptch^{Δep}* $n = 8$; lower panel). (C) Immunofluorescence staining of murine ear skin for Ly6G (red) and DAPI (blue). The arrows indicate Ly6G⁺ cells. E: epidermis, D: dermis, T: tumor mass, HF: hair follicle (scale bar 20 μm). (D) Representative immunohistochemical stainings of two human BCC skin sections for the neutrophil marker CD15 (brown) with nuclei stained in blue (scale bar 20 μm). Statistical analysis for all experiments was performed with Student's *t* test. *** $P < 0.001$ and **** $P < 0.0001$.

cells in skin samples of *Ptch^{fl/fl}* and *Ptch^{Δep}* mice by their CD11b and CD11c expression. Intriguingly, we found a pronounced increase in CD11b⁺ cells in mouse skin tumors (Fig. 3A), which we confirmed also in *SmoM2* mice (Fig. S6A). However, *SmoM2* mice showed a strong decrease in CD11c expression (Fig. S6A), while we did not see this prominent effect in *Ptch^{Δep}* mice (Fig. 3A).

Further analysis of CD11b⁺ cells using the neutrophil marker Ly6G and the natural killer (NK) cell marker NK1.1 revealed a noticeable recruitment of both innate immune cell populations in *Ptch^{Δep}* skin lesions (Fig. 3B). Ly6G⁺ cells were also increased in skin BCC-like lesions of *SmoM2* mice (Fig. S6B). To

better understand the putative role of neutrophils in BCC-like lesions, we first performed immunofluorescence staining of Ly6G⁺ cells in skin samples of *Ptch^{fl/fl}* and *Ptch^{Δep}* mice. We found most of the Ly6G⁺ cells to be located in the peri-tumoral region with only rare cells within the tumor nest itself (Fig. 3C).

Similarly, staining of human BCC samples for the neutrophil marker CD15 revealed CD15⁺ cells in the stromal compartment of human BCC tumors (Fig. 3D).

Since Fan *et al.* [64] have provided evidence that in *SmoM2* BCC mice Ly6G⁺ CD11b⁺ cells represent myeloid-derived suppressor cells (MDSCs) with immunosuppressive function, we analyzed Ly6G⁺/

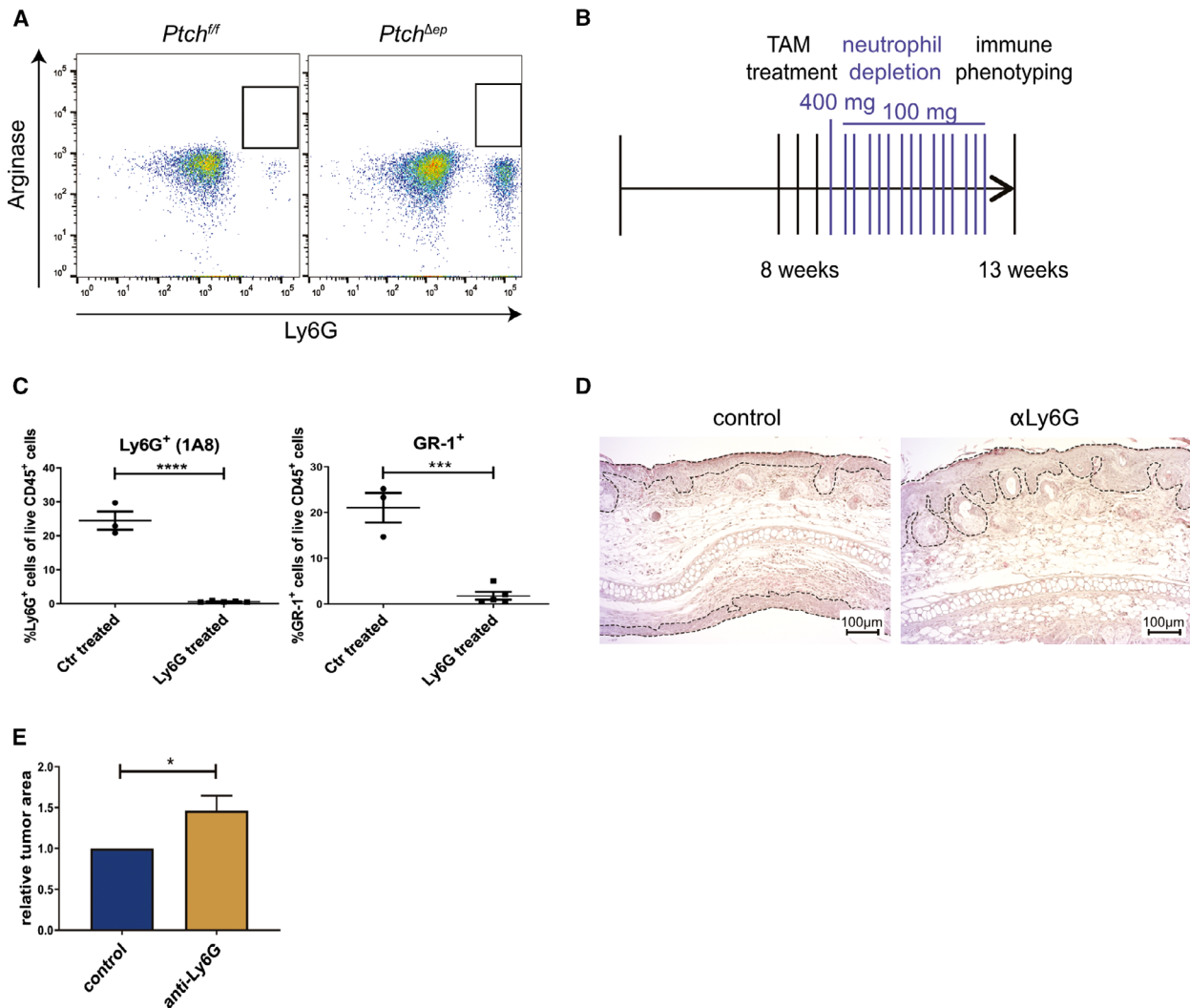


Fig. 4. Neutrophil depletion in BCC mice accelerates tumor growth. (A) Representative flow cytometry analysis plots of arginase staining in *Ptch^{Δep}* and *Ptch^{fl/fl}* mouse skin (*Ptch^{fl/fl}* $n = 2$ and *Ptch^{Δep}* $n = 4$). (B) Treatment schedule for neutrophil depletion in *K14CreER^{T2};Ptch^{fl/fl}* mice previously injected with TAM. (C) Flow cytometry analysis of murine skin for Ly6G or Gr-1 expression verifying efficient depletion of neutrophils (control $n = 3$, anti-Ly6G $n = 5$). (D) Representative H&E staining comparing tumor development in ear skin of *Ptch^{Δep}* mice not depleted (left) or depleted (right) of neutrophils during BCC progression. The dashed lines mark the tumor area (scale bar 100 μm). (E) Quantification of the tumor area in the ear skin of *Ptch^{Δep}* mice not depleted (control, $n = 3$) or depleted (anti-Ly6G, $n = 3$) of neutrophils during BCC progression. Statistical analysis for all experiments was performed with Student's *t* test, and for (E), the error bar indicates the SD. * $P < 0.05$, *** $P < 0.001$ and **** $P < 0.0001$.

CD11b⁺ cells of *Ptch^{Δep}* mice for the MDSC marker arginase (for antibody validation see Fig. S7). As shown in Fig. 4A, Ly6G⁺/CD11b⁺ cells of *Ptch^{Δep}* mice did not express the MDSC marker arginase, suggesting that tumor lesions of *Ptch^{Δep}* mice are infiltrated by neutrophils rather than MDSCs (Fig. 4A). To shed light on the role of tumor-infiltrating neutrophils in BCC, we next depleted *Ptch^{Δep}* mice of neutrophils by injecting anti-Ly6G depletion antibody (clone 1A8; Fig. 4B) and proved successful depletion

of neutrophils in the skin by flow cytometry (Fig. 4C). Intriguingly, depletion of neutrophils enhanced the growth of tumor lesions in *Ptch^{Δep}* mice (Fig. 4D,E), suggesting that neutrophils, known for their tumor-promoting function in a variety of malignant entities [65], may constitute a yet unknown component of the antitumoral immune response in BCC. Future studies are required to better understand the possible anti-cancer activity of neutrophils in the context of HH/GLI-driven BCC.

4. Discussion

The continuous growth and spread of malignant cells depend on the generation of an immunosuppressive microenvironment to prevent an efficient antitumoral immune response. The restoration of the immune response for instance by the use of checkpoint inhibitors has marked a breakthrough in cancer therapy with yet unprecedented success in responding patients [26]. A high mutational burden of cancer cells has been shown to correlate with the clinical response and success of immunotherapy using checkpoint inhibitors [45]. Given the exceptionally high mutational burden of human BCC [47], we here hypothesized that (a) HH/GLI-induced human BCC is immunogenic, (b) HH/GLI signaling establishes an immunosuppressive tumor microenvironment, and (c) HH/GLI-driven BCC is susceptible to immunotherapy. To investigate in detail the poorly defined role of HH/GLI in the process of immune evasion, we used genetic mouse models of BCC that closely mimic the genetics of driver mutations in human BCC. In the present study, we show that active epidermal HH/GLI signaling is a potent inducer of immunosuppressive mechanisms such as the accumulation of Tregs, the upregulation of immune checkpoints and the production of immunosuppressive growth factors and cytokines including IL10 and TGF β within the tumor lesions. Although we did not determine the *in vivo* source of these immunosuppressive signals, it is well possible that these key immunosuppressive factors derive directly from cancer cells in response to active HH/GLI. This is supported by previous studies showing that Sonic HH/GLI signaling can induce IL10 expression in a murine model of colitis and pancreatitis. Similarly, overexpression of active GLI2 in T cells can cell-autonomously enhance IL10 and TGF β expression [66–69]. In line with the expression of IL10 and TGF β , we show increased numbers of Treg cells in *Ptch^{Aep}* tumors, similar to human BCC, where Omland *et al.* [70] provided evidence that active HH/GLI signaling can induce Treg accumulation along with a strong increase of TGF β expression. Furthermore, Hanna *et al.* [71] have recently shown that HH/GLI signaling can drive Treg recruitment in breast cancer, while pathway inhibition reduced the number of Tregs in the tumor. Similar results were shown by Otsuka *et al.* for human BCC [72]. The high prevalence of Tregs within the tumor microenvironment is, thus, likely to constitute a major mechanism of immunosuppression by HH/GLI signaling in cancer.

In addition to an increased level of Treg cells, we demonstrated enhanced expression of the immune checkpoint molecules PD-1 and its cognate ligands

PD-L1 and PD-L2 in *Ptch^{Aep}* mouse tumors, with PD-L1 expressed preferentially on epithelial tumor cells and PD-1 on adjacent CD8⁺ and CD4⁺ T cells. This suggests that HH/GLI signaling in BCC can induce PD-L1 expression on tumor cells and, thereby, contribute to the suppression of infiltrating cytotoxic T cells directed against the tumor cells. Together with previous reports on the role of HH/GLI in gastric cancer showing PD-L1 upregulation by HH/GLI signaling [59,73], our findings in BCC suggest that HH/GLI-mediated induction of the PD-L1/PD-1 immune checkpoint may represent a more general mechanism of HH-mediated immune escape in cancer. Intriguingly, the increased expression in *Ptch^{Aep}* lesions of additional immune checkpoints such as Tigit and Tim3 (Fig. 2A) [54] points to a broader involvement of oncogenic HH/GLI signaling in the suppression of cytotoxic T cell responses, increasing the therapeutic opportunities for combination treatments with anti-HH and immune checkpoint inhibitors.

In agreement with our findings on immune checkpoint expression profiles of murine BCC-like lesions, first proof-of-concept studies support a therapeutic benefit of anti-PD-1 treatment for patients with advanced or metastatic and SMO inhibitor-resistant BCC [27,28,74]. These positive initial results underline the importance of predictive mouse models of BCC that allow the evaluation of innovative combination therapies including immunotherapeutics. Thus, our characterization of the immunological alterations in response to Hh/Gli activation in *Ptch^{Aep}* and *SmoM2* mouse models is crucial to understand the immune infiltration and cytokine/chemokine expression profiles in BCC-like skin lesions. It proves the usefulness of these mouse models to study in detail the pathologically relevant changes in the immune microenvironment of HH/GLI-induced BCC. However, the failure of *Ptch^{Aep}* mice to respond to anti-PD-1 immune checkpoint inhibitor therapy, which may be due to the absence of immunogenic mutations as shown by whole-exome sequencing, reveals the limitations of this common BCC mouse model for immunotherapy approaches. Unlike human BCC, murine BCC-like lesions displayed a moderately reduced number of T cells. We speculate that the decrease of T cells, particularly of CD8⁺ cells, may be a consequence of a lack of neoantigens and of increased levels of immunosuppressive cytokines in the tumor microenvironment, which may induce T cell anergy and apoptosis. The development of immunogenic murine BCC models is, therefore, paramount for future preclinical studies.

By staining human BCC, we revealed that these tumors could be subdivided into tumors with low and

high PD-L1 expression, respectively. In PD-L1 low tumors, the CD8⁺ T cell infiltration was mostly restricted to the peri-tumoral regions, while in PD-L1 high tumors CD8⁺ T cells were located in close proximity to the PD-L1-expressing tumor cells. Intriguingly, we detected PD-1 expression on both CD8 and CD4 T cells in the tumor stroma, including infiltration of the epithelial tumor compartment by CD8⁺PD1⁺ cells. It will be of interest to evaluate whether the stratification of patients into PD-L1 high/low or into high/low infiltration with CD8⁺PD1⁺/CD4⁺PD1⁺ T cells results in differential response rates to immune checkpoint blockers. The current lack of patient stratification and predictive markers may explain why the combined treatment of BCC patients with vismodegib and pembrolizumab did not yield a significant therapeutic benefit (trial ID: NCT02690948).

In addition to changes of the T cell populations, we also identified pronounced infiltration of BCC-like lesions by Ly6G⁺/Arginase^{neg} neutrophils, which was in agreement with the elevated expression of chemokines such as Ccl2 and Ccl3, two potent chemoattractants for myeloid cells [62,63]. Since the selective depletion of neutrophils accelerated tumor development in *Ptch^{Aep}* mice, we conclude that neutrophils, which we found to be mainly located in the tumor periphery, can fulfill antitumorogenic functions in HH/GLI-driven skin cancer. Although neutrophils are well known for their tumor-promoting function [35,75,76], evidence also suggests a critical contribution of neutrophils to the antitumoral immune response, reflecting their remarkable plasticity [77]. For instance, neutrophils have been shown to enhance MHC-I expression, thereby increasing the antitumoral response of adaptive immunity. Further, tumor-associated neutrophils can promote the proliferation of effector T cells and impede tumor progression by the release of pro-apoptotic TRAIL (reviewed in [65]). Whether these mechanisms account for the tumor-suppressive activity of neutrophils in murine BCC skin needs to be addressed in future studies. In this context, it is also noteworthy that Fan *et al.* have provided evidence that prenatal epidermal activation of *SmoM2* resulted in BCC-like lesions enriched for Ly6G^{pos} pro-tumorogenic MDSCs. Recruitment of MDSCs was inhibited by systemic chemical inhibition of Ccl2 receptor, resulting in reduced tumor growth [64]. However, in contrast to our data and studies on human BCC, *SmoM2* mice with prenatal Hh/Gli activation and MDSC enrichment did not show enhanced Treg numbers, which may point to subtle differences in the immune modulation of the distinct mouse models used.

5. Conclusion

Taken together, we conclude that the mere genetic activation of HH/GLI signaling in epidermal cells induces profound changes within the immune microenvironment of BCC-like lesions, thereby establishing a potent immunosuppressive milieu, which is likely to inhibit the antitumoral immune response against human BCC cells with high mutational burden. Therapeutic strategies directed against immunosuppressive mechanisms activated by HH/GLI including several checkpoint inhibitors warrant further evaluation. Our results also call for next-generation, immunogenic models of BCC to explore the full therapeutic potential of treatments including HH pathway inhibitors in combination with selected immunotherapeutic drugs.

Acknowledgements

We dedicate this work to our dear colleague Peter Hammerl, who sadly passed away during the course of this study. This work was supported by the Austrian Science Fund (FWF projects W1213 and P25629), the priority program Allergy-Cancer-Bionano Research Center of the University of Salzburg, and the Cancer Cluster Salzburg research grant of the County of Salzburg. The authors are grateful to the animal caretakers, to Drs. Angelika Stöcklinger, Walter Stoiber and Angela Zissler for methodical input and continuous support, to Drs. Gernot Posselt and Silja Wessler for help with microscopy and to Mag. Suzana Tesanovic and Mag. Dominik Elmer for help with the preparation of animals. Furthermore, the authors would like to express special thanks to Sabine Siller for technical support and Georg Stockmaier for critical reading of the manuscript.

Conflict of interest

The authors declare no conflict of interest.

Data accessibility

All reagents and material developed during the study will be made available to the scientific community for nonprofit use upon request.

Author contributions

SG-G, DO, ABS-N, DN, IKG, PS, and FA were responsible for the concept and experimental design. SG-G, DO, and DN performed the experiments. SG-G, DO, ABS-N, DN, NZ, IKG, PS, and FA analyzed

and interpreted the data. ABS-N, RW, DN, MW, AR, PH, RG, NZ, MS, IKG, and PS helped to develop the methodology. SG-G and FA wrote the manuscript. All authors read and approved the final manuscript.

Ethical approval

Human BCC specimen used for immunohistochemical analysis was analyzed and processed in accordance with the guidelines of the Austrian ethics committee. Animal studies were approved by the institution authorities and by the Federal Ministry of Science, Research and Economy (BMWF-66.012/0016-WF/V/3b/2015 and BMWF-66.011/0030-II/3b/2014).

References

- 1 Sekulic A & Von Hoff D (2016) Hedgehog pathway inhibition. *Cell* **164**, 831.
- 2 Epstein EH (2008) Basal cell carcinomas: attack of the hedgehog. *Nat Rev Cancer* **8**, 743–754.
- 3 Hahn H, Wicking C, Zaphiropoulos PG, Gailani MR, Shanley S, Chidambaram A, Vorechovsky I, Holmberg E, Unden AB, Gillies S *et al.* (1996) Mutations of the human homolog of *Drosophila* patched in the nevoid basal cell carcinoma syndrome. *Cell* **85**, 841–851.
- 4 Hui CC & Angers S (2011) Gli proteins in development and disease. *Annu Rev Cell Dev Biol* **27**, 513–537.
- 5 Johnson RL, Rothman AL, Xie J, Goodrich LV, Bare JW, Bonifas JM, Quinn AG, Myers RM, Cox DR, Epstein EH Jr *et al.* (1996) Human homolog of patched, a candidate gene for the basal cell nevus syndrome. *Science (New York, N.Y.)* **272**, 1668–1671.
- 6 Kasper M, Regl G, Frischauf AM & Aberger F (2006) GLI transcription factors: mediators of oncogenic Hedgehog signalling. *Eur J Cancer* **42**, 437–445.
- 7 Nilsson M, Undén AB, Krause D, Malmqwist U, Raza K, Zaphiropoulos PG & Toftgård R (2000) Induction of basal cell carcinomas and trichoepitheliomas in mice overexpressing GLI-1. *Proc Natl Acad Sci USA* **97**, 3438–3443.
- 8 Ruiz i Altaba A, Mas C & Stecca B (2007) The Gli code: an information nexus regulating cell fate, stemness and cancer. *Trends Cell Biol* **17**, 438–447.
- 9 Teglund S & Toftgård R (2010) Hedgehog beyond medulloblastoma and basal cell carcinoma. *Biochem Biophys Acta* **1805**, 181–208.
- 10 Xie J, Murone M, Luoh SM, Ryan A, Gu Q, Zhang C, Bonifas JM, Lam CW, Hynes M, Goddard A *et al.* (1998) Activating smoothed mutations in sporadic basal-cell carcinoma. *Nature* **391**, 90–92.
- 11 Oro AE, Higgins KM, Hu Z, Bonifas JM, Epstein EH & Scott MP (1997) Basal cell carcinomas in mice overexpressing sonic hedgehog. *Science (New York, N.Y.)* **276**, 817–821.
- 12 Grachtchouk M, Mo R, Yu S, Zhang X, Sasaki H, Hui CC & Dlugosz AA (2000) Basal cell carcinomas in mice overexpressing Gli2 in skin. *Nat Genet* **24**, 216–217.
- 13 Atwood SX, Whitson RJ & Oro AE (2014) Advanced treatment for basal cell carcinomas. *Cold Spring Harb Perspect Med* **4**, a013581.
- 14 Axelson M, Liu K, Jiang X, He K, Wang J, Zhao H, Kufirin D, Palmby T, Dong Z, Russell AM *et al.* (2013) U.S. Food and Drug Administration approval: vismodegib for recurrent, locally advanced, or metastatic basal cell carcinoma. *Clin Cancer Res* **19**, 2289–2293.
- 15 Casey D, Demko S, Shord S, Zhao H, Chen H, He K, Putman A, Helms W, Keegan P & Pazdur R (2017) FDA approval summary: sonidegib for locally advanced basal cell carcinoma. *Clin Cancer Res* **23**, 2377–2381.
- 16 Dlugosz A, Agrawal S & Kirkpatrick P (2012) Vismodegib. *Nat Rev Drug Discovery* **11**, 437–438.
- 17 Sekulic A, Migden MR, Basset-Seguín N, Garbe C, Gesierich A, Lao CD, Miller C, Mortier L, Murrell DF, Hamid O *et al.* (2017) Long-term safety and efficacy of vismodegib in patients with advanced basal cell carcinoma: final update of the pivotal ERIVANCE BCC study. *BMC Cancer* **17**, 332.
- 18 Atwood SX, Li M, Lee A, Tang JY & Oro AE (2013) GLI activation by atypical protein kinase C iota/lambda regulates the growth of basal cell carcinomas. *Nature* **494**, 484–488.
- 19 Atwood SX, Sarin KY, Whitson RJ, Li JR, Kim G, Rezaee M, Ally MS, Kim J, Yao C, Chang AL *et al.* (2015) Smoothed variants explain the majority of drug resistance in basal cell carcinoma. *Cancer Cell* **27**, 342–353.
- 20 Sharpe HJ, Pau G, Dijkgraaf GJ, Basset-Seguín N, Modrusan Z, Januario T, Tsui V, Durham AB, Dlugosz AA, Haverty PM *et al.* (2015) Genomic analysis of smoothed inhibitor resistance in basal cell carcinoma. *Cancer Cell* **27**, 327–341.
- 21 Tang JY, Mackay-Wiggan JM, Aszterbaum M, Yauch RL, Lindgren J, Chang K, Coppola C, Chanana AM, Marji J, Bickers DR *et al.* (2012) Inhibiting the hedgehog pathway in patients with the basal-cell nevus syndrome. *N Engl J Med* **366**, 2180–2188.
- 22 Whitson RJ, Lee A, Urman NM, Mirza A, Yao CY, Brown AS, Li JR, Shankar G, Fry MA, Atwood SX *et al.* (2018) Noncanonical hedgehog pathway activation through SRF-MKL1 promotes drug resistance in basal cell carcinomas. *Nat Med* **24**, 271–281.
- 23 Chen DS & Mellman I (2013) Oncology meets immunology: the cancer-immunity cycle. *Immunity* **39**, 1–10.

- 24 Okazaki T, Chikuma S, Iwai Y, Fagarasan S & Honjo T (2013) A rheostat for immune responses: the unique properties of PD-1 and their advantages for clinical application. *Nat Immunol* **14**, 1212–1218.
- 25 Pardoll D & Allison J (2004) Cancer immunotherapy: breaking the barriers to harvest the crop. *Nat Med* **10**, 887–892.
- 26 Wei SC, Duffy CR & Allison JP (2018) Fundamental mechanisms of immune checkpoint blockade therapy. *Cancer Discov* **8**, 1069–1086.
- 27 Chang ALS, Tran DC, Cannon JGD, Li S, Jeng M, Patel R, Van der Bokke L, Pague A, Brotherton R, Rieger KE *et al.* (2019) Pembrolizumab for advanced basal cell carcinoma: An investigator-initiated, proof-of-concept study. *J Am Acad Dermatol* **80**, 564–566.
- 28 Lipson EJ, Lilo MT, Ogurtsova A, Esandrio J, Xu H, Brothers P, Schollenberger M, Sharfman WH & Taube JM (2017) Basal cell carcinoma: PD-L1/PD-1 checkpoint expression and tumor regression after PD-1 blockade. *J Immunother Cancer* **5**, 23.
- 29 Mao J, Ligon KL, Rakhlin EY, Thayer SP, Bronson RT, Rowitch D & McMahon AP (2006) A novel somatic mouse model to survey tumorigenic potential applied to the Hedgehog pathway. *Can Res* **66**, 10171–10178.
- 30 Ramirez A, Page A, Gandarillas A, Zanet J, Pibre S, Vidal M, Tusell L, Genesca A, Whitaker DA, Melton DW *et al.* (2004) A keratin K5Cre transgenic line appropriate for tissue-specific or generalized Cre-mediated recombination. *Genesis* **39**, 52–57.
- 31 Curran MA, Montalvo W, Yagita H & Allison JP (2010) PD-1 and CTLA-4 combination blockade expands infiltrating T cells and reduces regulatory T and myeloid cells within B16 melanoma tumors. *Proc Natl Acad Sci USA* **107**, 4275–4280.
- 32 John LB, Devaud C, Duong CP, Yong CS, Beavis PA, Haynes NM, Chow MT, Smyth MJ, Kershaw MH & Darcy PK (2013) Anti-PD-1 antibody therapy potently enhances the eradication of established tumors by gene-modified T cells. *Clin Cancer Res* **19**, 5636–5646.
- 33 Mittal D, Young A, Stannard K, Yong M, Teng MW, Allard B, Stagg J & Smyth MJ (2014) Antimetastatic effects of blocking PD-1 and the adenosine A2A receptor. *Can Res* **74**, 3652–3658.
- 34 Ngo SF, Young A, Jacquilot N, Yamazaki T, Enot D, Zitvogel L & Smyth MJ (2015) A threshold level of intratumor CD8⁺ T-cell PD1 expression dictates therapeutic response to anti-PD1. *Can Res* **75**, 3800–3811.
- 35 Coffelt SB, Kersten K, Doornebal CW, Weiden J, Vrijland K, Hau CS, Versteegen NJ, Ciampricotti M, Hawinkels LJ, Jonkers J *et al.* (2015) IL17-producing $\gamma\delta$ T cells and neutrophils conspire to promote breast cancer metastasis. *Nature* **522**, 345–348.
- 36 Eberl M, Klingler S, Mangelberger D, Loipetzberger A, Damhofer H, Zoidl K, Schnidar H, Hache H, Bauer HC, Solca F *et al.* (2012) Hedgehog-EGFR cooperation response genes determine the oncogenic phenotype of basal cell carcinoma and tumour-initiating pancreatic cancer cells. *EMBO Mol Med* **4**, 218–233.
- 37 Li H & Durbin R (2010) Fast and accurate long-read alignment with Burrows-Wheeler transform. *Bioinformatics* **26**, 589–595.
- 38 McKenna A, Hanna M, Banks E, Sivachenko A, Cibulskis K, Kernytzky A, Garimella K, Altshuler D, Gabriel S, Daly M *et al.* (2010) The genome analysis toolkit: a MapReduce framework for analyzing next-generation DNA sequencing data. *Genome Res* **20**, 1297–1303.
- 39 Li H, Handsaker B, Wysoker A, Fennell T, Ruan J, Homer N, Marth G, Abecasis G & Durbin R (2009) The sequence alignment/map format and SAMtools. *Bioinformatics* **25**, 2078–2079.
- 40 Koboldt DC, Larson DE & Wilson RK (2013) Using VarScan 2 for germline variant calling and somatic mutation detection. *Curr Protoc Bioinformatics* **44**, 15.14.11–17.
- 41 Wang K, Li M & Hakonarson H (2010) ANNOVAR: functional annotation of genetic variants from high-throughput sequencing data. *Nucleic Acids Res* **38**, e164.
- 42 Robinson JT, Thorvaldsdottir H, Winckler W, Guttman M, Lander ES, Getz G & Mesirov JP (2011) Integrative genomics viewer. *Nat Biotechnol* **29**, 24–26.
- 43 Thorvaldsdottir H, Robinson JT & Mesirov JP (2013) Integrative Genomics Viewer (IGV): high-performance genomics data visualization and exploration. *Brief Bioinform* **14**, 178–192.
- 44 Seshan V & Olshen A (2019) DNACopy: DNA copy number data analysis. R package version 1.58.0. <https://doi.org/10.18129/B9.bioc.DNACopy>
- 45 Samstein RM, Lee CH, Shoushtari AN, Hellmann MD, Shen R, Janjigian YY, Barron DA, Zehir A, Jordan EJ, Omuro A *et al.* (2019) Tumor mutational load predicts survival after immunotherapy across multiple cancer types. *Nat Genet* **51**, 202–206.
- 46 Efremova M, Finotello F, Rieder D & Trajanoski Z (2017) Neoantigens generated by individual mutations and their role in cancer immunity and immunotherapy. *Front Immunol* **8**, 1679.
- 47 Bonilla X, Parmentier L, King B, Bezrukov F, Kaya G, Zoete V, Seplyarskiy VB, Sharpe HJ, McKee T, Letourneau A *et al.* (2016) Genomic analysis identifies new drivers and progression pathways in skin basal cell carcinoma. *Nat Genet* **48**, 398–406.
- 48 Biehs B, Dijkgraaf GJP, Piskol R, Alicke B, Boumahdi S, Peale F, Gould SE & de Sauvage FJ (2018) A cell identity switch allows residual BCC to survive Hedgehog pathway inhibition. *Nature* **562**, 429–433.
- 49 Sternberg C, Gruber W, Eberl M, Tesanovic S, Stadler M, Elmer DP, Schleiderer M, Grund S, Roos S, Wolff

- F *et al.* (2018) Synergistic cross-talk of hedgehog and interleukin-6 signaling drives growth of basal cell carcinoma. *Int J Cancer* **143**, 2943–2954.
- 50 Thibert C, Teillet MA, Lapointe F, Mazelin L, Le Douarin NM & Mehlen P (2003) Inhibition of neuroepithelial patched-induced apoptosis by sonic hedgehog. *Science (New York, N.Y.)* **301**, 843–846.
- 51 Barnes EA, Kong M, Ollendorff V & Donoghue DJ (2001) Patched1 interacts with cyclin B1 to regulate cell cycle progression. *EMBO J* **20**, 2214–2223.
- 52 Mougiakakos D, Choudhury A, Lladser A, Kiessling R & Johansson CC (2010) Regulatory T cells in cancer. *Adv Cancer Res* **107**, 57–117.
- 53 Takeuchi Y & Nishikawa H (2016) Roles of regulatory T cells in cancer immunity. *Int Immunol* **28**, 401–409.
- 54 Greil R, Hutterer E, Hartmann TN & Pleyer L (2017) Reactivation of dormant anti-tumor immunity – a clinical perspective of therapeutic immune checkpoint modulation. *Cell Commun Signal* **15**, 5.
- 55 Borghaei H, Paz-Ares L, Horn L, Spigel DR, Steins M, Ready NE, Chow LQ, Vokes EE, Felip E, Holgado E *et al.* (2015) Nivolumab versus docetaxel in advanced nonsquamous non-small-cell lung cancer. *N Engl J Med* **373**, 1627–1639.
- 56 Brahmer J, Reckamp KL, Baas P, Crinò L, Eberhardt WE, Poddubskaya E, Antonia S, Pluzanski A, Vokes EE, Holgado E *et al.* (2015) Nivolumab versus docetaxel in advanced squamous-cell non-small-cell lung cancer. *N Engl J Med* **373**, 123–135.
- 57 Postow MA, Chesney J, Pavlick AC, Robert C, Grossmann K, McDermott D, Linette GP, Meyer N, Giguere JK, Agarwala SS *et al.* (2015) Nivolumab and ipilimumab versus ipilimumab in untreated melanoma. *N Engl J Med* **372**, 2006–2017.
- 58 Robert C, Long GV, Brady B, Dutriaux C, Maio M, Mortier L, Hassel JC, Rutkowski P, McNeil C, Kalinka-Warzocho E *et al.* (2015) Nivolumab in previously untreated melanoma without BRAF mutation. *N Engl J Med* **372**, 320–330.
- 59 Chakrabarti J, Holokai L, Syu L, Steele NG, Chang J, Wang J, Ahmed S, Dlugosz A & Zavros Y (2018) Hedgehog signaling induces PD-L1 expression and tumor cell proliferation in gastric cancer. *Oncotarget* **9**, 37439–37457.
- 60 Jones PA, Ohtani H, Chakravarthy A & De Carvalho DD (2019) Epigenetic therapy in immune-oncology. *Nat Rev Cancer* **19**, 151–161.
- 61 Gaga M, Ong YE, Benyahia F, Aizen M, Barkans J & Kay AB (2008) Skin reactivity and local cell recruitment in human atopic and nonatopic subjects by CCL2/MCP-1 and CCL3/MIP-1 α . *Allergy* **63**, 703–711.
- 62 Griffith JW, Sokol CL & Luster AD (2014) Chemokines and chemokine receptors: positioning cells for host defense and immunity. *Annu Rev Immunol* **32**, 659–702.
- 63 Deshmane SL, Kremlev S, Amini S & Sawaya BE (2009) Monocyte chemoattractant protein-1 (MCP-1): an overview. *J Interferon Cytokine Res* **29**, 313–326.
- 64 Fan Q, Gu D, Liu H, Yang L, Zhang X, Yoder MC, Kaplan MH & Xie J (2014) Defective TGF- β signaling in bone marrow-derived cells prevents hedgehog-induced skin tumors. *Can Res* **74**, 471–483.
- 65 Galdiero MR, Varricchi G, Loffredo S, Mantovani A & Marone G (2018) Roles of neutrophils in cancer growth and progression. *J Leukoc Biol* **103**, 457–464.
- 66 Furler RL & Uittenbogaart CH (2012) GLI2 regulates TGF- β 1 in human CD4 $^+$ T cells: implications in cancer and HIV pathogenesis. *PLoS One* **7**, e40874.
- 67 Lee JJ, Rothenberg ME, Seeley ES, Zimdahl B, Kawano S, Lu WJ, Shin K, Sakata-Kato T, Chen JK, Diehn M *et al.* (2016) Control of inflammation by stromal Hedgehog pathway activation restrains colitis. *Proc Natl Acad Sci USA* **113**, E7545–E7553.
- 68 Papaioannou E, Yanez DC, Ross S, Lau CI, Solanki A, Chawda MM, Virasami A, Ranz I, Ono M, O’Shaughnessy RFL *et al.* (2019) Sonic Hedgehog signaling limits atopic dermatitis via Gli2-driven immune regulation. *J Clin Invest* **129**, 3153–3170.
- 69 Zhou X, Liu Z, Jang F, Xiang C, Li Y & He Y (2012) Autocrine Sonic hedgehog attenuates inflammation in cerulein-induced acute pancreatitis in mice via upregulation of IL-10. *PLoS One* **7**, e44121.
- 70 Omland SH, Nielsen PS, Gjerdrum LM & Gniadecki R (2016) Immunosuppressive environment in basal cell carcinoma: the role of regulatory T cells. *Acta Derm Venereol* **96**, 917–921.
- 71 Hanna A, Metge BJ, Bailey SK, Chen D, Chandrashekar DS, Varambally S, Samant RS & Shevde LA (2019) Inhibition of Hedgehog signaling reprograms the dysfunctional immune microenvironment in breast cancer. *Oncoimmunology* **8**, 1548241.
- 72 Otsuka A, Dreier J, Cheng PF, Nageli M, Lehmann H, Felderer L, Frew IJ, Matsushita S, Levesque MP & Dummer R (2015) Hedgehog pathway inhibitors promote adaptive immune responses in basal cell carcinoma. *Clin Cancer Res* **21**, 1289–1297.
- 73 Holla S, Stephen-Victor E, Prakhar P, Sharma M, Saha C, Udupa V, Kaveri SV, Bayry J & Balaji KN (2016) Mycobacteria-responsive sonic hedgehog signaling mediates programmed death-ligand 1- and prostaglandin E2-induced regulatory T cell expansion. *Sci Rep* **6**, 24193.
- 74 Ikeda S, Goodman AM, Cohen PR, Jensen TJ, Ellison CK, Frampton G, Miller V, Patel SP & Kurzrock R (2016) Metastatic basal cell carcinoma with amplification of PD-L1: exceptional response to anti-PD1 therapy. *NPJ Genom Med* **1**, 16037.

- 75 Fridlender ZG, Sun J, Kim S, Kapoor V, Cheng G, Ling L, Worthen GS & Albelda SM (2009) Polarization of tumor-associated neutrophil (TAN) phenotype by TGF- β : “N1” versus “N2” TAN. *Cancer Cell* **16**, 183–194.
- 76 Mantovani A (2009) The yin-yang of tumor-associated neutrophils. *Cancer Cell* **16**, 173–174.
- 77 Ponzetta A, Carriero R, Carnevale S, Barbagallo M, Molgora M, Perucchini C, Magrini E, Gianni F, Kunderfranco P, Polentarutti N *et al.* (2019) Neutrophils driving unconventional T cells mediate resistance against murine sarcomas and selected human tumors. *Cell* **178**, 346–360.e324.

Supporting information

Additional supporting information may be found online in the Supporting Information section at the end of the article.

Fig. S1. Altered immune phenotype of *SmoM2* mice. (A–D) Flow cytometry analysis of (A) CD3⁺ (*Smo*^{WT} $n = 7$, *SmoM2* $n = 6$) and CD3^{high} (*Smo*^{WT} $n = 7$, *SmoM2* $n = 7$) T cells, (B) CD4 and CD8 T cells in *Smo*^{WT} ($n = 5$) and *SmoM2* ($n = 7$) mice. (C, D) mRNA expression level of (C) *Foxp3* and (D) *Pd-1* in *Smo*^{WT} ($n = 3$) and *SmoM2* ($n = 3$) mice. For *Foxp3* expression analysis mice were harvested ~4 weeks (early, $n = 3$) and 12 weeks (late, $n = 3$) post Tamoxifen administration.

Fig. S2. BCC tumors reveal co-expression of PD-1 with CD4 and CD8 but not FoxP3. (A) Two representative immunohistochemical stainings of human BCC skin sections stained for FoxP3 (red) and PD-1 (brown), nuclei are stained in blue (scale bar 20 μ m). (B) Flow cytometry analysis of PD-1 expression on CD3⁺ T cells in *Ptch*^{fl/fl} ($n = 2$) and *Ptch*^{Aep} ($n = 4$) mice. (C) Representative immunohistochemical stainings of two human BCC skin sections for PD-1

(brown) with CD4 or CD8 (red), nuclei are stained in blue. White arrowheads indicate representative double positive cells (scale bar 20 μ m).

Fig. S3. Anti-Pd-1 blocking does not reduce skin cancer phenotype of *Patched*^{Aep} mice. (A) Quantification of the tumor area in the ear skin of *Ptch*^{Aep} mice untreated or treated with anti-PD-1 blocking antibodies during BCC progression ($n = 4$ per group). (B) Flow cytometry analysis of the skin after Pd-1 blocking ($n = 4$ per group).

Fig. S4. Mouse tumors exhibit no large structural genetic variations. Representative copy number variation (CNV) plot from mouse #2. CNV analysis reveals no deletions or amplifications.

Fig. S5. Altered cytokine and chemokine profile of *SmoM2*. Cytokine and chemokine profiles were determined *via* mRNA expression level of *Smo*^{WT} ($n = 4$, for *Il10* and *Ccl2* $n = 3$) and *SmoM2* mice ($n = 3$).

Fig. S6. Altered innate immunity in *SmoM2* mice. (A–D) Flow cytometry analysis of (A) CD11b (*Smo*^{WT} $n = 6$, *SmoM2* $n = 5$) and CD11c (*Smo*^{WT} $n = 4$, *SmoM2* $n = 3$) innate immune cells and (B) GR-1⁺ (*Smo*^{WT} $n = 4$, *SmoM2* $n = 4$) and NK1.1⁺ (*Smo*^{WT} $n = 3$, *SmoM2* $n = 3$) cells in *Smo*^{WT} and *SmoM2* mice.

Fig. S7. Validation of the arginase antibody. Representative flow cytometry plots of bone marrow-derived macrophages unstimulated or stimulated with Il4, a known inducer of arginase expression.

Table S1. Antibodies used for flow cytometry.

Table S2. Primer sequences used for qPCR of murine samples.

Table S3. qPCR primer list for *SmoM2* mice.

Table S4. Antibodies used for immunofluorescence and immunohistochemistry.

Table S5. Mutational landscape of tumors from *Ptch*^{Aep} mice.